Journal of Materials Chemistry A

Silver niobate based lead-free ceramics with high energy storage density

Journal:	*Journal of Materials Chemistry A*
Manuscript ID	TA-ART-01-2019-000995.R1
Article Type:	Paper
Date Submitted by the Author:	29-Mar-2019
Complete List of Authors:	Yan, Zhongna; State key Laboratory of Powder Metallurgy, Central South University Zhang, Dou; Central South University, State Key Laboratory of Powder Metallurgy Zhou, Xuefan; Central South University, State Key Laboratory of Powder Metallurgy Qi, He; Hefei University of Technology, Luo, Hang; Central South University, Zhou, Kechao; Central South University Abrahams, I.; Queen Mary, Chemistry Yan, Haixue; Queen Mary University of London, School of Engineering and Materials Science

Journal of Materials Chemistry A

ARTICLE

Silver niobate based lead-free ceramics with high energy storage density

Received 00th xx 20xx,
Accepted 00th xx 20xx

DOI: 10.1039/x0xx00000x

www.rsc.org/

Zhongna Yan,[a,b] Dou Zhang,*[a] Xuefan Zhou,[a] He Qi,[a] Hang Luo,[a] Kechao Zhou,[a] Isaac Abrahams,*[b] and Haixue Yan*[c]

Antiferroelectrics that display double ferroelectric hysteresis loops have been extensively studied because of their excellent energy storage density compared to normal ferroelectrics and linear dielectrics. Although excellent properties have been achieved in lead-based antiferroelectrics, a feasible replacement for them is urgently needed, with growing concerns on use of lead-containing materials. This work focuses on fabricating $AgNbO_3$-based lead-free antiferroelectric ceramics achieved by co-doping of Bi^{3+} on the A-site and Zn^{2+} on the B-site in $AgNbO_3$. These dopants were specifically chosen because of their demonstrated positive influence on energy density and efficiency in $AgNbO_3$ and other lead-free ferroelectric ceramics. The new $AgNbO_3$-based ceramics exhibit a high recoverable energy storage density of 4.6 J/cm^3, which is one of the highest values for a lead-free ceramic system reported to date. Co-doping of Bi^{3+} on the A-site and Zn^{2+} on the B-site is found to shift the freezing temperature, T_f, to below room temperature stabilizing the antiferroelectric state at room temperature. The increased dielectric breakdown strength, E_b, and electrical displacement, D_m, together with enhanced forward and backward fields are responsible for the high energy storage density. This work shows that a targeted co-doping approach can be an effective strategy for the development of high-performance ceramic capacitors for energy storage applications.

1. Introduction

The development of high pulsed power technologies has allowed for their application in a variety of areas such as power transmission and distribution, aircraft, electric vehicles, and pulsed power weapons.[1-3] Compared to currently available energy storage devices, such as batteries and supercapacitors, dielectric capacitors, with their ultrafast charge/discharge rates and excellent fatigue resistance, are the core components of pulsed power devices.[4-6] However, for applications in energy storage, dielectric capacitors are limited by their low energy storage density.[7] Enhancements in energy storage density of the constituent dielectric material would allow for reductions in volume and weight of these devices.[7-9]

The recoverable energy storage density (W_{rec}) of a dielectric material is given by:[10]

$$W_{\mathrm{rec}} = \int_{D_r}^{D_m} E dD \quad (1)$$

where D_m, D_r, and E are the maximum electrical displacement, remnant electrical displacement and applied electric field, respectively. Thus, large D_m, small D_r and large E are necessary to obtain high energy density suitable for energy storage applications. A schematic illustration of the energy storage mechanism for antiferroelectrics is given in the supporting information as Figure S1. Generally, dielectric materials for energy storage are divided into four types: linear dielectrics, normal ferroelectrics (FEs), relaxor ferroelectrics and antiferroelectrics (AFEs).[11] Amongst these, AFEs display double hysteresis loops in their electric displacement-electric field diagrams, with characteristics of large D_m and small D_r and are considered to be one of the best candidates for energy storage applications.[12] For AFEs, increasing both the forward field E_F (from AFE to FE) and the backward field E_B (from FE to AFE) are also crucial in enhancing energy storage density.[13]

La-doped lead zirconium titanate ceramics exhibit the highest known W_{rec} for a ceramic of 6.4 J/cm^3.[14] However, due to growing concerns in recent years, associated with environmental protection and human health, a suitable replacement for lead-containing materials is urgently needed.[11,15] Various lead-free systems have been explored such as those based on $Bi_{0.5}Na_{0.5}TiO_3$ (BNT),[16] $BaTiO_3$ (BT),[17] $K_{0.5}Na_{0.5}NbO_3$ (KNN)[18] and $KTa_{1-x}Nb_xO_3$ (KTN).[19] $AgNbO_3$ is a lead-free AFE ceramic that displays double ferroelectric hysteresis loops, with a large field induced polarization (52.0 μC/cm^2) under high electric field (220 kV/cm), resulting in excellent energy storage performance.[20] However, there are

a. State Key Laboratory of Powder Metallurgy, Central South University, South Lushan Road, Changsha, 410083, Hunan Province, China. E-mail: dzhang@csu.edu.cn
b. School of Biological and Chemical Sciences, Queen Mary University of London, Mile End Road, London, E1 4NS, UK. E-mail: i.abrahams@qmul.ac.uk
c. School of Engineering and Materials Sciences, Queen Mary University of London, Mile End Road, London, E1 4NS, UK. E-mail: h.x.yan@qmul.ac.uk
† Electronic Supplementary Information (ESI) available. See DOI: 10.1039/x0xx00000x

still many open questions regarding details of the local structure and phase transitions in $AgNbO_3$, including the nature of the freezing temperature T_f.[10,21]

A-site doping is a method for altering the value of D_m, for example, in the case of Bi^{3+} or Pb^{2+} doping, large values of D_m can be achieved, which has been explained by hybridization between Bi or Pb 6s and O 2p orbitals.[22-25] Tian *et al.* reported that A-site doping by Bi^{3+} can lead to an enhancement of antiferroelectricity in $AgNbO_3$-based ceramics and the T_f can be lowered to below room temperature with increasing dopant concentration.[21] Zhao *et al.* reported that the AFE performance of $AgNbO_3$ ceramics can be significantly enhanced by incorporating Mn^{4+}, Ta^{5+} or W^{6+} on the B-site,[13,26,27] indicating that E_F and E_B can be increased in $AgNbO_3$ ceramics through B site doping.

When used as a B-site dopant, Zn^{2+}, has been shown to successfully increase field induced electrical displacement in other perovskite based ferroelectric ceramics such as $Bi_{0.5}Na_{0.5}TiO_3$ and $BaTiO_3$;[28,29] to the best of our knowledge, the effects of Zn^{2+} doping into $AgNbO_3$ have not been investigated. We have previously shown that A-site doping by Bi^{3+} in $AgNbO_3$ successfully increases energy density and efficiency.[21] In this work, we use a strategy of simultaneous A and B site doping of $AgNbO_3$ by Zn^{2+} to increase D_m and Bi^{3+} to shift E_F and E_B to higher electric field, and adjust T_f to below room temperature. The new solid solution system $(1\text{-}x)AgNbO_3\text{-}xBi(Zn_{2/3}Nb_{1/3})O_3$ presented here is specifically designed to achieve high energy storage density. This targeted approach has yielded a material with a recoverable energy storage density of 4.6 J/cm^3, which is one of the highest known values reported for a lead-free ceramic system to date.

2. Experimental

$(1\text{-}x)AgNbO_3\text{-}xBi(Zn_{2/3}Nb_{1/3})O_3$ (x = 0.000, 0.005, 0.010 and 0.030) ceramics, abbreviated as (1-x)AN-xBZN, were obtained by a conventional solid-state reaction method. Stoichiometric amounts of Ag_2O (99.7%), Nb_2O_5 (99.99%), ZnO (99%) and Bi_2O_3 (99.9%) were ground in anhydrous ethanol for 24 h using a planetary ball mill at 280 rpm in a nylon jar. After drying, the blended powders were calcined at 850 °C in a tube furnace for 6 h in flowing O_2. The calcined powders were re-milled for 24 h in anhydrous ethanol. After drying, they were blended with 5 wt% PVA solution and were pressed into disks of 12 mm diameter and 1.0-1.5 mm thickness under 180 MPa for 1.5 min. After burning off the PVA at 600 °C for 2 h, the disks were sintered at temperatures between 1070 - 1110 °C for 6 h in flowing O_2, followed by cooling to room temperature. The heating/cooling rate and the O_2 flow rate were 5 °C/min and 0.5 L/min, respectively.

The density of the sintered samples was measured by the Archimedes method in water. The morphology of polished and thermally etched (at 1130 °C for 30 min) surfaces was observed by field emission scanning electron microscopy (FESEM, Nova NanoSEM230, USA) and grain size measurements made using the Image J software.[30] X-ray powder diffraction (XRD, D8 Advance, Bruker) was used to determine the phase structure using Cu-Kα radiation (λ = 1.5418 Å). Raman spectra were measured using a LabRAM HR800 spectrometer (Horiba JobinYvon, Paris, France). Transmission electron microscopy (TEM) images and selected-area electron diffraction (SAED) patterns of the samples were recorded using a Titan G2 60-300 electron microscope (FEI, USA), with energy dispersive spectroscopy (EDS) carried out using an EDS system (Oxford Instruments, UK) on the same microscope. For the TEM characterization, the samples were mechanically ground and polished down to 60 µm in thickness, followed by ion thinning to electron transparency. Piezoelectric force microscopy (PFM) measurements were performed using an atomic force microscope (NanoManTM VS) with a conductive Pt/Ir-coated Si cantilever (SCM-PIT). For the PFM measurements, samples were ground and polished down to a thickness of 80 µm and polarized in advance under an electric field of 100 kV/cm. Measurements were performed using a tip bias voltage of 12 V.

For electrical characterization, Ag electrodes were applied and fired on both parallel surfaces of the samples. The temperature dependent permittivity was measured using an LCR meter (Agilent E4980A) connected to a computer-controlled furnace from 1 kHz to 1 MHz on heating and cooling. The frequency dependent permittivity was measured using an LCR meter (Agilent 4284A) at room temperature. The electric displacement-electric field (*D-E*) and current- electric field (*I-E*) hysteresis loops for these samples with Ag electrodes (2-3 mm in diameter) on both parallel surfaces were measured in silicone oil using a ferroelectric measurement system (aixACCT, TF Analyzer2000, Germany) at 1 Hz. The samples were lapped down to a thickness of *ca.* 0.23 mm for the low and high electric field *D-E* loop measurements to study the phase transitions induced by the electric field. The differential permittivity (dD/dE) versus electric field loops were obtained from the *D-E* loops. The values of breakdown strength were analysed with a two-parameter Weibull distribution function using the following equation: [31]

$$P(E) = 1\text{-}\exp[-(E_b/E_0)^{\beta}] \qquad (2)$$

where $P(E)$ is the cumulative probability of electric failure, β is a shape parameter, and E_0 represents the characteristic breakdown strength required for 63.2% of the tested samples to fail.

3. Results and discussion

2.1 Structural characterization

SEM images of (1- x)AN-xBZN ceramics are shown in Figure 1a-d. All ceramics possess dense microstructures with relative densities above 95%. The average grain size decreases with increasing dopant level, Figure 1a1-d1. While this phenomenon has been seen before in $AgNbO_3$-based ceramics,[26] in the present case it is likely due to the lower sintering temperatures used for the doped samples (1100 °C for pure AN, 1090 °C for x = 0.005 and x = 0.010, and 1070 °C for x = 0.030). The TEM EDX mapping images of the x = 0.010 composition (Figure S2) show a uniform distribution of the constituent elements Ag, Bi, Nb, Zn and O.

Figure 2a shows the XRD patterns of crushed pellets of the studied ceramics, with detail of the weaker reflections shown in Figure 2b-e. The patterns are in good agreement with those of

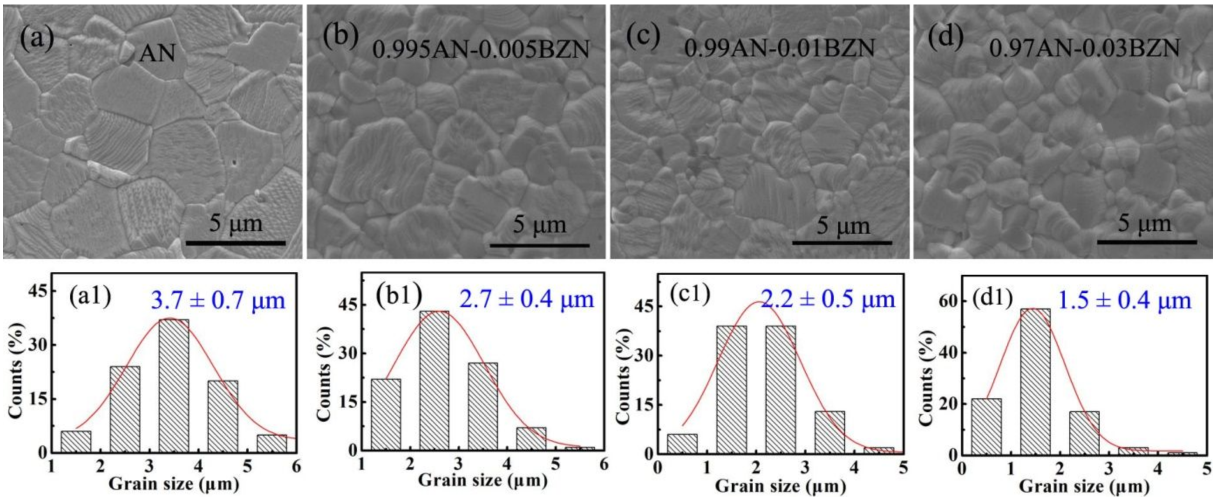

Figure 1 (a-d) SEM images and (a1-d1) grain size distributions of (1-*x*)AN-*x*BZN ceramics. Grain sizes were measured from 100 randomly selected grains in the corresponding SEM image.

$AgNbO_3$ (PDF #70-4738). There are very small changes in the unit cell parameters (Figure S3). While there is a slight general decrease in *a* and *b* parameters from $x = 0.000$ to $x = 0.030$, the *c*-parameter increases over this range, giving an overall increase in volume at $x = 0.030$ compared to pure $AgNbO_3$. These very small changes in lattice parameters are to be expected, not only because of the low levels of substitution, but also due to the fact that while the ionic radius of Zn^{2+} is larger than that of Nb^{5+} (r = 0.74 Å and 0.64 Å, respectively for the ions in 6 coordinate geometry), the ionic radius of Bi^{3+} is smaller than that of Ag^{+} (r = 1.17 Å and 1.28 Å, respectively for the ions in 8 coordinate geometry).[32] For the $x = 0.030$ composition this would equate to an overall change in volume of 0.05%, compared to unsubstituted $AgNbO_3$, which is close to the observed value of

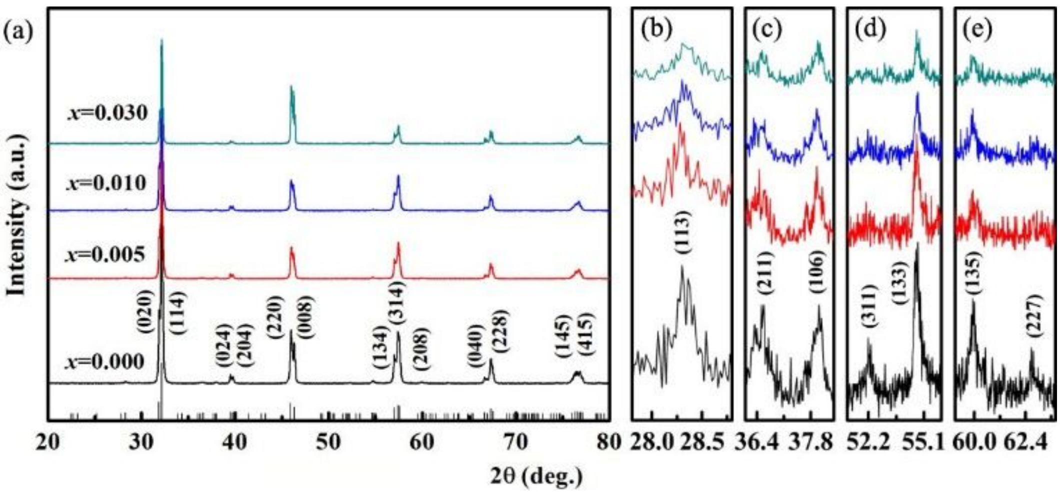

Figure 2 XRD patterns of (1-*x*) AN-*x*BZN crushed ceramics: (a) full patterns and (b) to (e) detail of weaker reflections. Miller indices corresponding to the *Pbcm* cell are shown with reflection positions indicated by markers in (a).

0.06%. The solid solution formula is such that electroneutrality is maintained through a balance of substitutional point defects rather than vacancies or interstitials (Equation 3).

$$3Ag_{Ag}^{X} + 2Nb_{Nb}^{X} \xrightarrow{Bi,Zn} 3Bi_{Ag}^{\bullet\bullet} + 2Zn_{Nb}^{'''} \quad (3)$$

Rietveld analysis was used to investigate the room temperature structure of the $x = 0.010$ composition. As discussed in the work of Tian *et al.*,[10] both polar and non-polar models were tested in space groups $Pb2_1m$ and *Pbcm*, respectively. The fitted diffraction profiles for these two models are compared in Figure S4. Both models, fit the data well, with similar reliability factors. Bearing in mind the increased number of parameters in the $Pb2_1m$ model, it does not offer a significantly improved fit over the *Pbcm* model, generating similar reliability factors. Thus it may be concluded that the average structure is adequately described as being centrosymmetric i.e. AFE. Bright-field TEM images and selected-area electron diffraction (SAED) patterns of the $x = 0.010$ composition viewed along the [001], [100], [22-1], and [04-1] zone axes of the orthorhombic cell are shown in Figure 3.

Crystallites are seen to be multi-domain and composed of micron-sized domain blocks, Figure 3a-c. Although the average structure from the Rietveld analysis is centrosymmetric, it has been reported that in $AgNbO_3$ lower symmetry FE regions (*$Pb2_1m$*) within the average AFE matrix may exist.[10, 13, 33] In general, the appearance of (*h0l*) or (*00l*) reflections with $l = 2n + 1$ in SAED images indicates the existence of the polar phase. The (003) reflection, as indicated by the red arrows in Figure 3e and 3g, is clear evidence for the presence of the $Pb2_1m$ polar phase. Therefore, while the majority of the crystallites in the $x = 0.010$ ceramic are non-polar, low concentrations of polar crystallites appear to be present.

Generally, the phase stability of a perovskite structure can be evaluated according to the perovskite tolerance factor (t), which is given by equation 4, where R_A, R_B, and R_O are the ionic radii of A-and B-site cations, and the oxygen anion, respectively.[34]

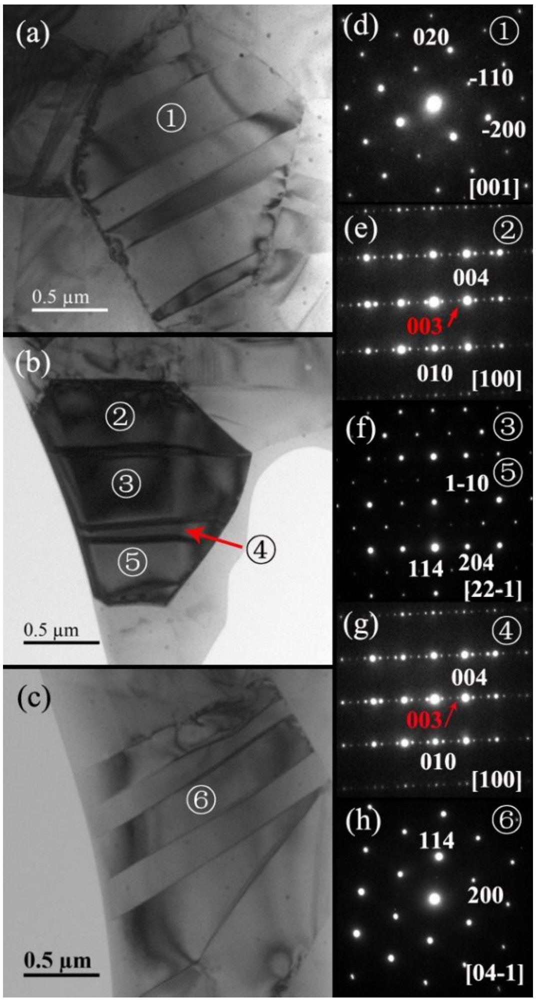

Figure 3 TEM images of 0.99AN-0.01BZN ceramics: (a)-(c) overview bright-field images showing the domains; (d) SAED patterns taken from the domain labeled ① in (a); (e)-(g) SAED patterns taken from the domains labeled ②-⑤ in (b); (h) SAED patterns taken from the domains labeled ⑥ in (c).

$$t = \frac{R_A + R_O}{\sqrt{2}(R_B + R_O)} \quad (4)$$

The FE phase is stabilized when $t > 1$, while the AFE phase is stabilized when $t < 1$. The substitution of Bi^{3+} for Ag^+, and Zn^{2+} for Nb^{5+} gives t values in the range 0.7999 to 0.8007 for the studied compositions, which is in the range of AFE phase stability.

Figure 4 shows the fitted Raman spectra of the studied (1-*x*)AN-*x*BZN ceramics. The spectrum of the $x = 0.000$ composition is in good agreement with those in previous studies.[35] Low wavenumber bands are associated with vibrations of the Nb^{5+} and Ag^+ cations (< 92 cm^{-1} and 200 to 350 cm^{-1}) and tilting of the NbO_6 octahedra at around 105 cm^{-1}. The higher wavenumber bands are associated with bending and stretching modes υ_1, υ_2, υ_4, υ_5 of the NbO_6 octahedra. On substitution of Ag^+ by Bi^{3+} and Nb^{5+} by Zn^{2+}, all bands weaken and broaden until at $x = 0.030$

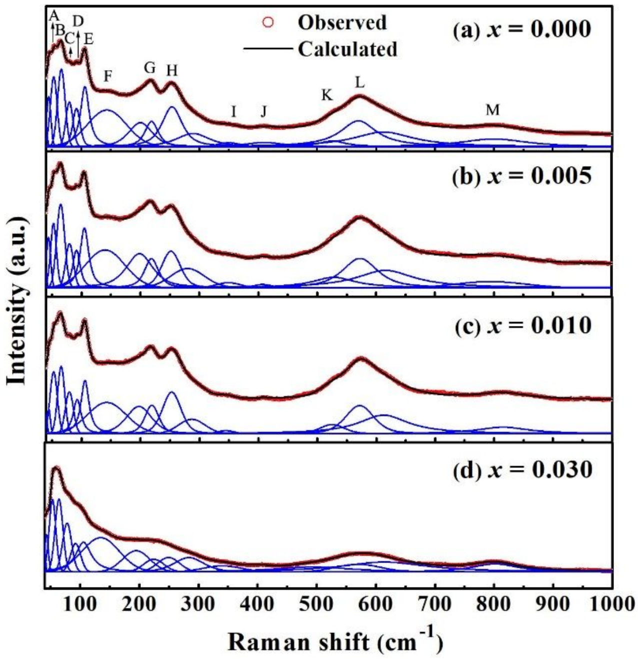

Figure 4 Fitted Raman spectra of (1-*x*)AN-*x*BZN ceramics.

only very broad features are seen in the spectrum.

Spectral broadening such as that seen can be attributed to increasing disorder in the system with increasing level of substitution and is consistent with the observed general increase in unit cell volume. This would be expected to result in an increasing range of low symmetry environments for the B site cations with increasing *x*-value. Similar behaviour was observed in the $AgNb_{1-x}Ta_xO_3$ system, where it was attributed to the lower polarizability of the substituting cation as well as a reduction in the correlation length of the displacements.[13] In the present case, while the polarizability of Zn^{2+} (1.29 Å^3) is very much lower than that of Nb^{5+} (3.10 Å^3), that of Bi^{3+} (3.95 Å^3) is much larger than that of Ag^+ (1.78 Å^3),[29] making the B-site cations on average less sensitive to the applied electric field. In Raman spectra this change in polarizability has the effect of weakening or enhancing modes. This is clearly visible in the E mode of the $x = 0.030$ composition, associated with tilting of the niobate octahedra, which is significantly weakened with respect to other modes. This suggests that the structure of this composition is above its T_f temperature.

Table 1 Raman shift and possible assignment of phonon modes of $AgNbO_3$ at room temperature.

Phonon mode	Raman shift [cm^{-1}]	Assignment	Reference
A	52.7	Ag^+/Nb^{5+}	36, 37
B	66.1	Ag^+/Nb^{5+}	36, 37
C	79.5	Ag^+/Nb^{5+}	36, 37
D	91.4	Ag^+	20, 37
E	104.8	NbO_6 tilting	36
F	141.7	?	35
G	218.5	?	35
H	253.8	$E_g(Nb) + A_{1g}(Nb)$	35, 37
I	349.5	Nb^{5+}	35
J	410.0	T_{2g} (υ_5) and/or T_{1u} (υ_4)	35, 36
K	523.6	$E_g(\upsilon_2)$	35
L	569.0	A_{1g} (υ_1) and E_g (υ_2)	35
M	803.5	A_{1g} (υ_1)	35

2.2 Dielectric response

Figure 5a-d shows the temperature dependence of relative permittivity and dielectric loss of (1-*x*)AN-*x*BZN ceramics over the frequency range 10 kHz to 1 MHz, from ambient temperature up to 500 °C on heating. Plots for sub-ambient temperatures are given in the supporting information as Figure S5. Several dielectric anomalies can be observed in Figure 5a, corresponding to the known phase transitions of pure $AgNbO_3$.[20] Dielectric anomalies at ca. 50 °C and ca. 260 °C are associated with the $M_1 \rightarrow M_2$ and $M_2 \rightarrow M_3$ phase transitions, respectively, which maintain the (a^-, b^-, c^+)/(a^-, b^-, c^-) octahedral tilting system throughout,[38] although the nature of these transitions is not yet fully understood.[10, 38] An anomaly in the dielectric loss spectrum at ca. 170 °C, that has only a very weak corresponding feature in the permittivity spectrum is ascribed to the freezing temperature, T_f (the critical temperature where the antipolar dipoles are frozen as cations order).[38, 39] The jump to a permittivity maximum near 350 °C, followed by a shoulder at around 400 °C are attributed to the *Pbcm* $\rightarrow$ *Cmcm* and *Cmcm* $\rightarrow$ to *P4/mbm* phase transitions, respectively. These involve changes in the octahedral tilting system of (a^-, b^-, c^+)/(a^-, b^-, c^-) $\rightarrow$ (a^0, b^-, c^+) $\rightarrow$ (a^0, b^0, c^+), respectively.[38] Apart from that

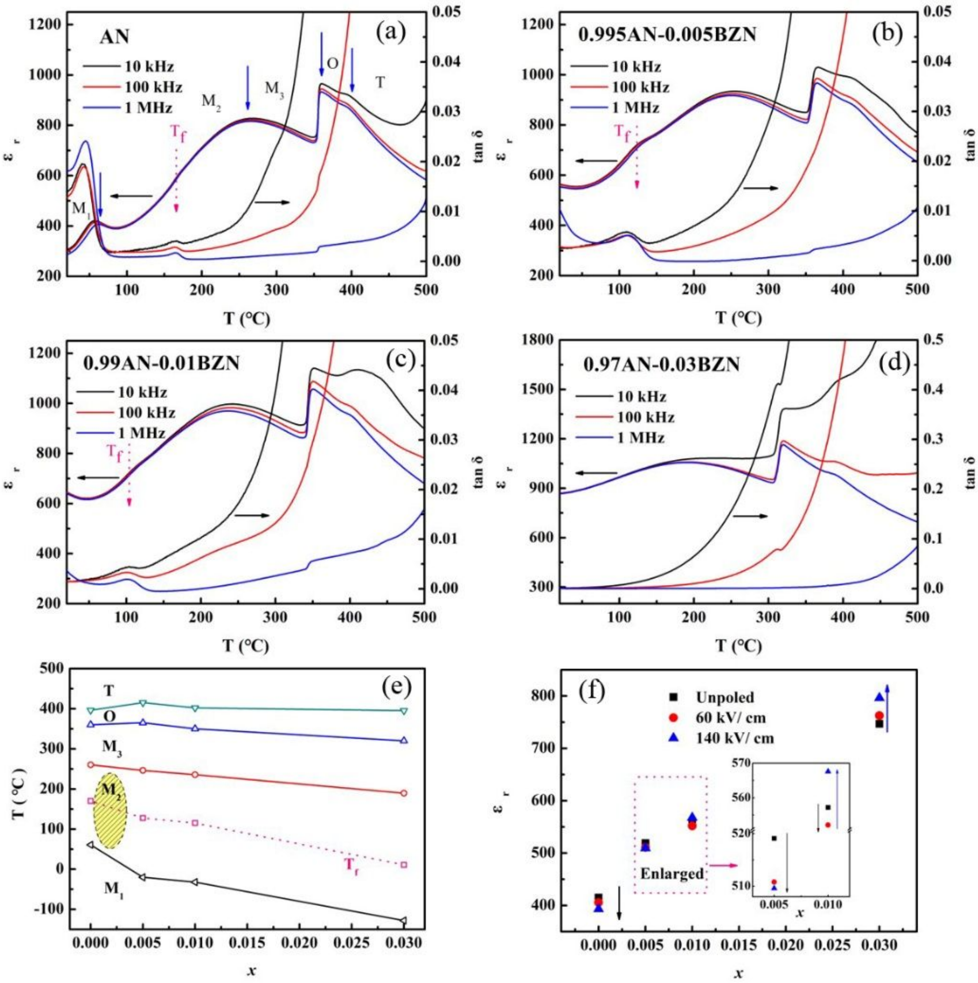

Figure 5 (a-d) Temperature dependence of relative permittivity and dielectric loss of (1-*x*)AN-*x*BZN ceramics from 10 kHz to 1MHz, (e) Phase diagram plotted at 1 kHz, (f) BZN concentration dependence of relative permittivity of (1-*x*)AN-*x*BZN ceramics plotted from frequency dependence of relative permittivity before and after poling at 1 MHz.

associated with the *Cmcm* → to *P4/mbm* transition, all dielectric anomalies show a general decrease in temperature with increasing *x*-value (Figure 5e), with the $M_1 \rightarrow M_2$ transition shifting to below room temperature. For the *x* = 0.030 composition, T_f is also shifted to below room temperature. Thus at ambient temperature, $AgNbO_3$ is present as the M_1 phase, while the doped compositions are in the M_2 phase either below T_f (*x* = 0.005 and 0.010) or above T_f (*x* = 0.030). Figure 5f shows the changes in relative permittivity before and after poling. For all samples, the relative permittivity increased with increasing *x*-value. For the *x* = 0.000 and *x* = 0.005 compositions, relative permittivity shows a small decrease after successive polarization under low (60 kV/cm) and high electric fields (140 kV/cm). In contrast, at *x* = 0.030 the relative permittivity increased on successive polarization under low and high electric fields. In the case of the *x* = 0.010 composition, intermediate behaviour is observed, with a decrease in relative permittivity on initial polarization at low field, followed by an increase at high field. The same trends were observed in multiple samples of the different compositions.

2.3 Electrical polarization response and energy storage performance

Figure 6 shows the low field (60 kV/cm) ferroelectric *D-E* and *I-E* loops measured at 1 Hz for (1-*x*)AN-*x*BZN ceramics. In agreement with the findings of Tian *et al.*,[10] two current peaks at $E_1 \approx 3$ kV/cm and $E_2 \approx 25$ kV/cm are observed in the *I-E* loop of the $AgNbO_3$ ceramic (Figure 6a), which have been attributed to FE domain switching behaviour and the field induced transition from ferrielectric (FIE) to ferroelectric states.[21,38] These current peaks gradually diminish with increasing *x*-value. Indeed, the E_1 peak is no longer evident in the *I-E* loop of the *x* = 0.005 composition (Figure 6b), while the E_2 peak, which is related to the field induced polar phase, broadens and shifts to lower field with increasing *x*-value, eventually disappearing at *x* = 0.030. Thus co-doping of $AgNbO_3$ appears to decrease the T_f temperature as previously noted for Bi doped $AgNbO_3$.[21] However, the D_{max} gradually increases with increasing doping level, which suggests that Zn doping causes an increase in the field induced electric displacement in the doped compositions. This is likely to be associated with a greater field induced distortion. Similar effects were observed in Zn^{2+} doped $Bi_{0.5}Na_{0.5}TiO_3$ and $BaTiO_3$.[28, 29]

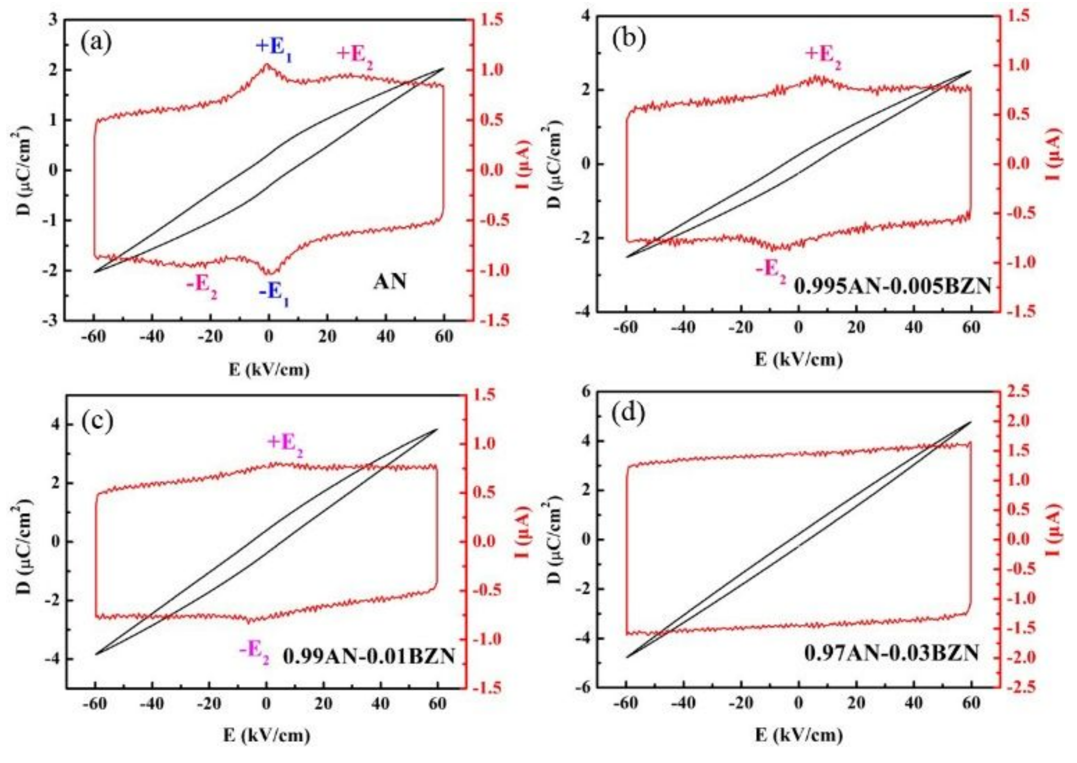

Figure 6 Low electric field ferroelectric *D-E* and *I-E* loops measured at 1 Hz for (1-*x*)AN-*x*BZN ceramics.

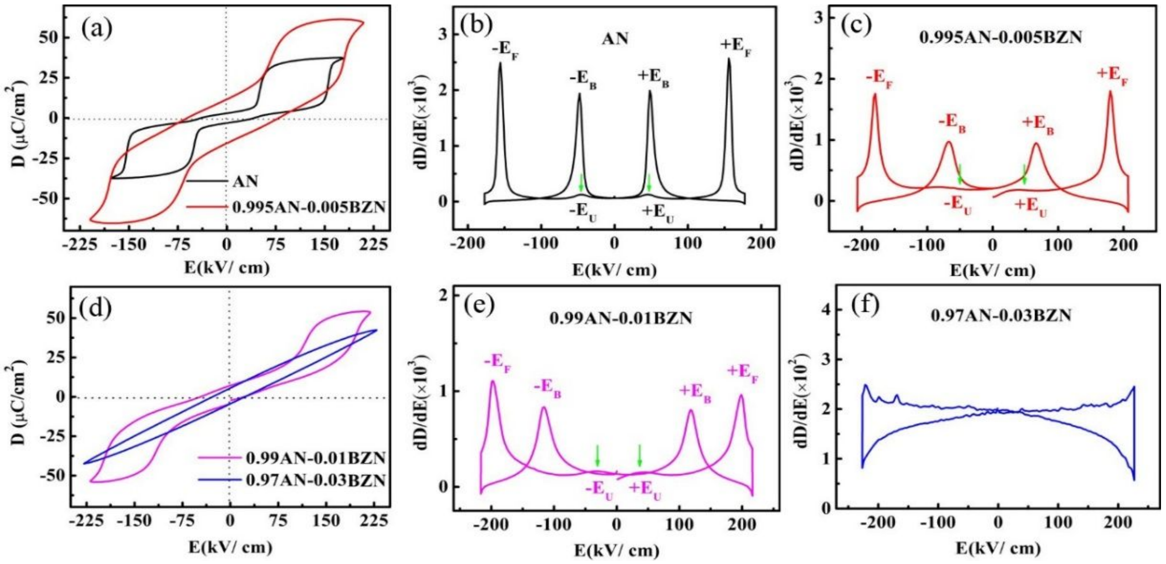

Figure 7 High electric field ferroelectric *D-E* (a and d) and *dD/dE-E* loops (b, c, e, and f) measured at 1 Hz for (1-*x*)AN-*x*BZN ceramics.

As discussed above, doping causes T_f to shift to lower temperature. Therefore, for the x = 0.030 composition, the M_2 phase present at room temperature is above the dipole freezing temperature, while for the x = 0.005 and 0.010 compositions the M_2 phase present at room temperature is below T_f. In undoped $AgNbO_3$, the decrease in relative permittivity on poling may be attributed to a decrease in FE domain wall density after being poled under *DC* field. As the concentration of FE domains decreases with increasing *x*-value, poling eventually results in an increase in permittivity as it induces the growth of new polar regions within a predominantly AFE matrix.[40] For the x = 0.010 composition, the initial decrease in permittivity is attributed to the decrease in FE domain wall density, while the increase in permittivity at higher field arises from field induced ferrielectric regions. Indeed, it is known that a strong E_2 peak can be induced at high field in $AgNbO_3$.[10] The *I-E* loop of the x = 0.030 composition exhibits near linear dielectric behaviour, which suggests that the structure of the room temperature phase (i.e. above T_f) is AFE and agrees with the lack of current peaks associated with domain switching events (E_1) and the field induced ferrielectric phase (E_2) in the *I-E* loop (Figure 6d).

The low field phase transition of the studied ceramics can be further characterized by the piezoresponse (PR) phase-voltage hysteresis and amplitude-voltage loops (Figure S6). Local butterfly with two minima and phase angle loops for the undoped material are characteristic of FE behavior.[41] Similar loops are seen for the x = 0.005 composition, confirming a significant FE contribution. As the dopant level increases, the FE contribution diminishes and hysteresis is minimized. V shaped curves are still observed, but now with a single minimum, corresponding to field induced polarization changes due to the higher applied field of the PFM tip.

Figure 7 exhibits the high electric field ferroelectric *D-E* and *dD/dE-E* loops of the as-prepared ceramics. Compositions with $x \leq$ 0.010 show double-like hysteresis loops, typical of AFE or AFE-like behaviour. Four sharp peaks are clearly seen in the *dD/dE-E* loops of compositions with $x \leq$ 0.010, as previously seen for the undoped $AgNbO_3$ ceramic;[21] two peaks, denoted $\pm E_F$ at higher field represent the electric forward field, at which the initial state is converted to the ferroelectric state, while two peaks at lower field denoted $\pm E_B$, represent the electric backward field at which the FE state is converted to the AFE state. In contrast, the x = 0.030 composition exhibits a near-linear hysteresis loop and the *dD/dE-E* loop shows no significant current peaks, suggesting much higher fields are required to drive the transition from AFE to FE states.

Table 2 summarizes the energy storage properties of the studied ceramics. With increasing *x*-value the electric field induced transition peaks E_F and E_B shift to higher electric field, consistent with the inhibition of local polar ordering by doping, resulting in the favouring of the AFE state.[21,38] Additionally, the difference (ΔE) between E_F and E_B decreases with increasing *x*-value, which is favourable for higher efficiency in energy storage. Close inspection of the *dD/dE-E* loops reveals weak peaks at around ± 50 kV/cm denoted $\pm E_U$. These have previously been observed in the parent compound, but their exact origin remains unclear.

Table 2 Energy storage properties of (1-*x*)AN-*x*BZN ceramics.

Samples	D_m [μC/cm²]	D_r [μC/cm²]	E_F [kV/cm]	E_B [kV/cm]	ΔE [kV/cm]	E_{max} [kV/cm]	W_{rec} [J/cm³]	η [%]
AN	37.3 ± 0.1	3.6 ± 0.1	158 ± 0.5	47 ± 0.5	111 ± 0.5	180	1.9 ± 0.1	35.2 ± 0.1
0.995AN-0.005BZN	59.3 ± 0.1	11.3 ± 0.1	178 ± 0.5	69 ± 0.5	109 ± 0.5	210	3.3 ± 0.1	31.2 ± 0.1
0.99AN-0.01BZN	53.8 ± 0.1	7.0 ± 0.1	198 ± 0.5	118 ± 0.5	80 ± 0.5	220	4.6 ± 0.1	57.5 ± 0.1
0.97AN-0.03BZN	42.4 ± 0.1	5.3 ± 0.1	-	-	-	230	3.7 ± 0.1	68.1 ± 0.1

Journal of Materials Chemistry A

ARTICLE

Average E_b values determined from the fitted Weibull plots (Figure S7a)[31] are in good agreement with the E_{max} values in Table 2. The improvement in E_b with increasing x-value is possibly due to the reduced grain size. Indeed, Tunkasiri *et al.* proposed an empirical relationship between grain size in the micron range and dielectric breakdown strength in $BaTiO_3$ ceramics:[42]

$$E_\mathrm{b} \propto \frac{1}{\sqrt{G}} \tag{5}$$

where G is the grain size. Similar results were also reported in MgO ceramics with smaller grains of sub-micron size by Beauchamp *et al.*.[43] As seen in Figure S7b, there is a reasonable correlation between E_b and grain size in the present system.

The maximum electric displacement, D_m, increases from 37.3 μC/cm^2 for pure $AgNbO_3$ to 59.3 μC/cm^2 for the x =0.005 composition and then decreases with increasing dopant level (Figure 7a Table 2). The same trend is seen for the remnant electric displacement (D_r), increasing from 3.6 μC/cm^2 for pure $AgNbO_3$ to 5.3 μC/cm^2 for the x = 0.030 composition, with a maximum value of 11.3 μC/cm^2 for the x = 0.005 composition. Compared to the lower field measurements, at high field, D_r increases in all samples. For compositions below x = 0.030 this can be attributed to the strong transition from FIE to FE states below T_f. In the case of the x = 0.030 composition, Figure 7f shows a sharp current peak at the highest field, suggesting the change in D_r is associated with a conductivity contribution.[44] The difference (ΔD) between the maximum electrical displacement (D_m) and remnant electrical displacement (D_r) is higher than that of pure $AgNbO_3$ for all the doped compositions.

As seen in Table 2, the doped ceramics show enhanced energy storage density, compared to undoped $AgNbO_3$, mainly due to the increased dielectric breakdown strength. The maximum W_{rec} of 4.6 J/cm^3 is achieved for the x = 0.010 composition, due to the increased E_F and E_B values as well as the large D_m (53.8 μC/cm^2) value (Figure 8a).

The energy storage efficiency η can be calculated as follows:

$$\eta = \frac{W_\mathrm{rec}}{W_\mathrm{rec} + W_\mathrm{loss}} \tag{6}$$

where the recoverable energy density (W_{rec}) and energy density loss (W_{loss}) are represented by the blue and the light brown areas, respectively (Figure S1). In this work, the η values show an increasing trend with increasing x-value as shown in Figure 8a. Amongst the studied compositions the best overall energy storage performance is shown by the x = 0.010 composition, with a high W_{rec} value of 4.6 J/cm^3 and η of 57.5%. The maximum energy storage density achieved in this ceramic is higher than in almost any other lead-free ceramic reported to date (Figure 8b) including KNN, BT, BNT, BST and AN based materials, and is 2.4 times larger than that of pure $AgNbO_3$. This high energy density is obtained at a lower field than that required to achieve similar energy densities in KNN based ceramics. These features make Bi,Zn co-doped $AgNbO_3$ ceramics a potential candidate for energy storage applications.

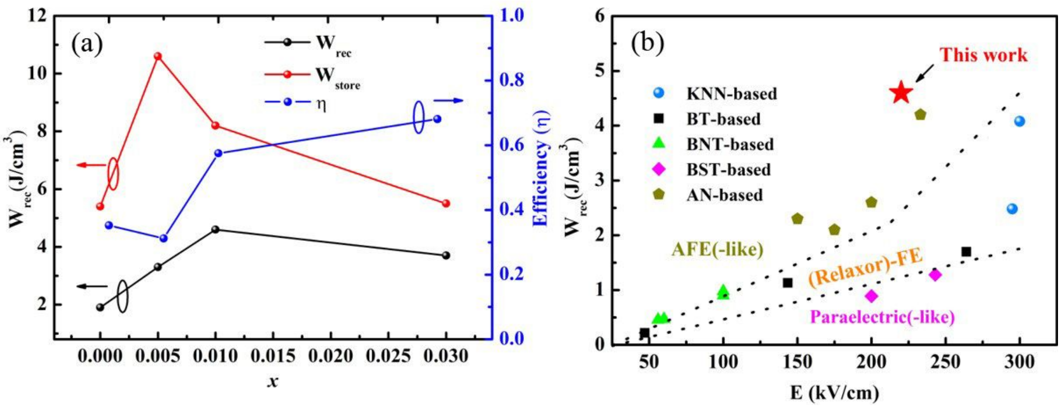

Figure 8 (a) Energy storage density (W) and efficiency (η) of (1-x)AN-xBZN ceramics and (b) comparison of recoverable energy density (W_{rec}) in 0.99AN-0.01BZN ceramic with that in other reported lead-free systems: $(K_{0.5}Na_{0.5})NbO_3$-based (Qu *et al.*,[45] and Shao *et al.*[24]), $BaTiO_3$-based (Wu *et al.*,[46] Wang *et al.*,[47] and Yuan *et al.*[48]), $Bi_{0.5}Na_{0.5}TiO_3$-based (Li *et al.*,[49] Xu *et al.*,[50] Ding *et al.*,[51] and Gao *et al.*[52]), $(Ba_{0.4}Sr_{0.6})TiO_3$-based (Song *et al.*,[53] and Zhang *et al.*[54]), and $AgNbO_3$-based (Tian *et al.*,[10, 21] and Zhao *et al.*[13, 27]).

Conclusions

In this work, increasing dopant concentration and decreasing grain size lead to improvements in dielectric breakdown strength. This allows for a higher applied electric field, which is beneficial to the improvement of the energy storage density. A large recoverable energy density of 4.6 J/cm^3, which is 2.4 times larger than that of pure $AgNbO_3$, has been achieved in 0.99AN-0.01BZN ceramic. Co-doping of Bi^{3+} and Zn^{2+} into $AgNbO_3$ stabilizes AFE behaviour, with the non-polar *Pbcm* phase dominant for the 0.99AN-0.01BZN ceramic. This stability can be explained by the decrease of the freezing temperature T_f to below room temperature. The enhanced maximum electrical displacement (D_m) is proposed to be due to the Zn^{2+} doping on the B-site and is likely to be associated with greater field induced distortion. The increased forward and backward electric fields (E_F and E_B), as well as the enhanced maximum electrical displacement (D_m) are responsible for the improved energy storage properties, making the (1-x)AN-xBZN solid solution a promising lead-free candidate for high performance ceramic capacitors for energy storage applications.

Conflicts of interest

There are no conflicts of interest to declare.

Acknowledgements

This work was financially supported by National Natural Science Foundation of China (51672311), Science and Technology Project of Hunan Province, China (no. 2016WK2022), and supported by the State Key Laboratory of Powder Metallurgy, Central South University, Changsha, China.

References

1. B. Chu, X. Zhou, K. Ren, B. Neese, M. Lin, Q. Wang, F. Bauer and Q. M. Zhang, *Science*, 2006, **313**, 334-336.
2. H. Pan, J. Ma, J. Ma, Q. Zhang, X. Liu, B. Guan, L. Gu, X. Zhang, Y.J. Zhang, L. Li, Y. Shen, Y. H. Lin and C. W. Nan, *Nature Communications*, 2018, **9**, 1813.
3. J. Wu, A. Mahajan, L. Riekehr, H. Zhang, B. Yang, N. Meng, Z. Zhang and H. Yan, *Nano Energy*, 2018, **50**, 723-732.
4. D. Zhang, W. Liu, R. Guo, K. Zhou and H. Luo, *Advanced Science*, 2018, **5**, 1700512.
5. L. F. Chen, Y. Feng, H. W. Liang, Z. Y. Wu and S. H. Yu, *Advanced Energy Materials*, 2017, **7**, 1700826.
6. Y. Zhang, Y. Wang, S. Qi, S. Dunn, H. Dong and T. Button, *Applied Physics Letters*, 2018, **112**, 202904.
7. B. Luo, X. Wang, E. Tian, H. Song, H. Wang and L. Li, *Acs Applied Materials & Interfaces*, 2017, **9**, 19963-19972.
8. H. Palneedi, M. Peddigari, G. T. Hwang, D. Y. Jeong and J. Ryu, *Advanced Functional Materials*, 2018, **28**, 1803665.
9. H. Luo, S. Chen, L. H. Liu, X. F. Zhou, C. Ma, W. W. Liu and D. Zhang, *Acs Sustainable Chemistry & Engineering*, 2019, **7**, 3145-3153.
10. Y. Tian, L. Jin, H. Zhang, Z. Xu, X. Wei, E. D. Politova, S. Y. Stefanovich, N. V. Tarakina, I. Abrahams and H. Yan, *Journal of Materials Chemistry A*, 2016, **4**, 17279-17287.
11. Z. Yao, Z. Song, H. Hao, Z. Yu, M. Cao, S. Zhang, M. T. Lanagan and H. Liu, *Advanced Materials*, 2017, **29**, 1601727.
12. B. Xu, J. Iniguez and L. Bellaiche, *Nature Communications*, 2017, **8**, 15682.
13. L. Zhao, Q. Liu, J. Gao, S. Zhang and J. F. Li, *Advanced Materials*, 2017, **29**, 1701824.
14. L. Zhang, S. Jiang, B. Fan and G. Zhang, *Journal of Alloys and Compounds*, 2015, **622**, 162-165.
15. Q. Yuan, G. Li, F. Z. Yao, S. D. Cheng, Y. Wang, R. Ma, S. B. Mi, M. Gu, K. Wang, J. F. Li and H. Wang, *Nano Energy*, 2018, **52**, 203-210.
16. A. Mahajan, H. Zhang, J. Wu, E. V. Ramana, M. J. Reece and H. Yan, *Journal of Physical Chemistry C*, 2017, **121**, 5709-5718.
17. Y. Tan, G. Viola, V. Kovale, C. Yu, A. Mahajan, J. Zhang, H. Zhang, X. Zhou, N. V. Tarakinac, H. Yan, *Journal of the European Ceramic Society*, 2019, **39**, 2064-2075.
18. M. Eriksson, H. Yan, M. Nygren, M. J. Reece and Z. Shen, *Journal of Materials Research*, 2010, **25**, 240-247.
19. Y. Wu, J. Li, H. Bai, Y. Hong, K. Z. Shi, Z. X. Zhou, R. Y. Guo and A. S. Bhalla, *Applied Physics Letters*, 2017, **111**, 242902.
20. D. Fu, M. Endo, H. Taniguchi, T. Taniyama and M. Itoh, *Applied Physics Letters*, 2007, **90**, 252907.
21. Y. Tian, L. Jin, H. Zhang, Z. Xu, X. Wei, G. Viola, I. Abrahams and H. Yan, *Journal of Materials Chemistry A*, 2017, **5**, 17525-17531.
22. J. Wang, J. B. Neaton, H. Zheng, V. Nagarajan, S. B. Ogale, B. Liu, D. Viehland, V. Vaithyanathan, D. G. Schlom, U. V. Waghmare, N. A. Spaldin, K. M. Rabe, M. Wuttig and R. Ramesh, *Science*, 2003, **299**, 1719-1722.
23. R. E. Cohen, *Nature*, 1992, **358**, 136-138.
24. T. Shao, H. Du, H. Ma, S. Qu, J. Wang, J. Wang, X. Wei and Z. Xu, *Journal of Materials Chemistry A*, 2017, **5**, 554-563.
25. M. Zhou, R. Liang, Z. Zhou and X. Dong, *Journal of Materials Chemistry A*, 2018, **6**, 17896-17904.
26. L. Zhao, J. Gao, Q. Liu, S. Zhang and J. F. Li, *Acs Applied Materials & Interfaces*, 2018, **10**, 819-826.
27. L. Zhao, Q. Liu, S. Zhang and J. F. Li, *Journal of Materials Chemistry C*, 2016, **4**, 8380-8384.
28. Y. Yao, Y. Li, N. N. Sun, J. H. Du, X. W. Li, L. W. Zhang, Q. W. Zhang and X. H. Hao, *Ceramics International*, 2018, **44**, 5961-5966.
29. A. Jain, A. K. Panwar and A. K. Jha, *Ceramics International*, 2017, **43**, 1948-1955.
30. H. Luo, J. Roscow, X. Zhou, S. Chen, X. Han, K. Zhou, D. Zhang and C. R. Bowen, *Journal of Materials Chemistry A*, 2017, **5**, 7091-7102.
31. E. Tuncer, D. R. James, I. Sauers, A. R. Ellis and M. O. Pace, *Journal of Physics D-Applied Physics*, 2006, **39**, 4257-4268.
32. R. D. Shannon, *Acta Crystallographica*, 2015, **32**, 751-767.
33. M. Yashima, S. Matsuyama, R. Sano, M. Itoh, K. Tsuda and D. Fu, *Chemistry of Materials*, 2011, **23**, 1643-1645.
34. D. I. Woodward, J. Knudsen and I. M. Reaney, *Physical Review B*, 2005, **72**, 4110.
35. H. U. Khan, K. Alam, M. Mateenullah, T. Blaschke and B. S. Haq, *Journal of the European Ceramic Society*, 2015, **35**, 2775-2789.
36. A. Kania, K. Roleder, G. E. Kugel and M. D. Fontana, *Journal of Physics C-Solid State Physics*, 1986, **19**, 9-20.
37. M. K. Niranjan, K. G. Prasad, S. Asthana, S. Rayaprol and V. Siruguri, *Journal of Physics D-Applied Physics*, 2015, **48**, 215303.
38. I. Levin, V. Krayzman, J. C. Woicik, J. Karapetrova, T. Proffen, M. G. Tucker and I. M. Reaney, *Physical Review B*, 2009, **79**, 104113.
39. A. Kania and J. Kwapulinski, *Journal of Physics-Condensed Matter*, 1999, **11**, 8933-8946.
40. G. Shirane, E. Sawaguchi and Y. Takagi, *Physical Review*, 1951, **84**, 476-481.
41. S. Mukherjee, A. Roy, S. Auluck, R. Prasad, R. Gupta and A. Garg, *Physical Review Letters*, 2013, **111**, 087601.
42. T. Tunkasiri and G. Rujijanagul, *Journal of Materials Science Letters*, 1996, **15**, 1767-1769.
43. E. Beauchamp, *Journal of the American Ceramic Society*, 1971, **54**, 484-487.
44. H. Yan, F. Inam, G. Viola, H. Ning, H. Zhang, Q. Jiang, T. Zeng,

Z. Gao and M. J. Reece, *Journal of Advanced Dielectrics,* 2010, **01**, 107-118.
45. B. Qu, H. Du and Z. Yang, *Journal of Materials Chemistry C*, 2016, **4**, 1795-1803.
46. L. Wu, X. Wang, H. Gong, Y. Hao, Z. Shen and L. Li, *Journal of Materials Chemistry C*, 2015, **3**, 750-758.
47. T. Wang, L. Jin, C. Li, Q. Hu and X. Wei, *Journal of the American Ceramic Society*, 2015, **98**, 559-566.
48. Q. Yuan, F. Yao, Y. Wang, R. Ma and H. Wang, *Journal of Materials Chemistry C*, 2017, **5**, 9552-9558.
49. F. Li, K. Yang, X. Liu, J. Zou, J. Zhai, B. Shen, P. Li, J. Shen, B. Liu, P. Chen, K. Zhao and H. Zeng, *Scripta Materialia*, 2017, **141**, 15-19.
50. Q. Xu, H. Liu, L. Zhang, J. Xie, H. Hao, M. Cao, Z. Yao and M. T. Lanagan, *Rsc Advances*, 2016, **6**, 59280-59291.
51. J. Ding, Y. Liu, Y. Lu, H. Qian, H. Gao, H. Chen and C. Ma, *Materials Letters*, 2014, **114**, 107-110.
52. F. Gao, X. Dong, C. Mao, W. Liu, H. Zhang, L. Yang, F. Cao and G. Wang, *Journal of the American Ceramic Society*, 2011, **94**, 4382-4386.
53. Z. Song, H. Liu, S. Zhang, Z. Wang, Y. Shi, H. Hao, M. Cao, Z. Yao and Z. Yu, *Journal of the European Ceramic Society*, 2014, **34**, 1209-1217.
54. Q. Zhang, L. Wang, J. Luo, Q. Tang and J. Du, *Journal of the American Ceramic Society*, 2009, **92**, 1871-1873.